Performance of an MEG Adaptive-Beamformer Technique in the Presence of Correlated Neural Activities: Effects on Signal Intensity and Time-Course Estimates

Kensuke Sekihara*, Srikantan S. Nagarajan, David Poeppel, and Alec Marantz

***Abstract*—The influence of temporarily correlated source activities on neuromagnetic reconstruction by adaptive beamformer techniques was investigated. It is known that the spatial filter weight of an adaptive beamformer cannot perfectly block correlated signals. This causes two major influences on the reconstruction results: time course distortions and reductions in reconstructed signal intensities. Our theoretical analysis and numerical experiments both showed that the reduction in signal intensity for sources with a medium degree of correlation is small. The time-course distortion for such sources, however, may be discernible. Our analysis also showed that the magnitude correlation coefficient between two correlated sources can be accurately estimated by using the beamformer outputs. A method of retrieving the original time courses using estimated correlation coefficients was developed. Our numerical experiments demonstrated that reasonably accurate time courses can be retrieved from considerably distorted time courses even when the signal-to-noise ratio is low.**

***Index Terms*—Adaptive beamformer, biomagnetism, functional neuroimaging, magnetoencephalographic (MEG) inverse problems, magnetoencephalography, neuromagnetic signal processing.**

I. Introduction

THE goal of neuromagnetic imaging is to visualize neural activities at a fine time resolution in the order of milliseconds, and to provide functional information about brain dynamics [1], [2]. Toward this goal, a number of algorithms for reconstructing spatio-temporal source activities from magnetoencephalographic (MEG) measurements have been developed. Among such algorithms, a class of techniques called an adaptive beamformer have attracted great interest recently. Adaptive-beamformer techniques were originally developed in the fields of array signal processing, including radar, sonar, and seismic exploration [3]. Since first introduced by Robinson *et al.* [4], they have been successfully applied to neuromagnetic source reconstruction problems [5]–[9]. The details of adaptive beamformer techniques, as well as their comparison to least-squares-based source-reconstruction techniques such as the minimum-norm method [10], are given in [11].

Adaptive-beamformer techniques, however, require an implicit assumption that the time courses of the source activities are orthogonal to each other; i.e., all source activities are completely uncorrelated [12]. This assumption may not necessarily hold in regard to neuromagnetic measurements. In general, cortical and subcortical activities are supposed to be more or less partially correlated. Indeed, this correlation itself has become an active research target [13]–[15] because the correlation between the neural activities is considered to represent some sort of functional connectivity between different regions in the brain [16]. Therefore, when applying adaptive-beamformer techniques, we should be aware of how robust they are to the source correlation, and what kind of influences arise when they are used to reconstruct correlated sources.

This paper attempts to answer these questions. It is known that the weight vector of adaptive beamformers cannot perfectly block correlated signals. This causes two major influences on the source-reconstruction results: distortion in time-course estimates and reduction in reconstructed source intensities. We performed theoretical analysis under the condition that two correlated sources exist and derived theoretical relationships between the degree of these influences and the degree of source correlations. We also develop a method of retrieving the original time courses when two sources are correlated. In this paper, Section II briefly reviews existing adaptive-beamformer techniques for neuromagnetic reconstruction. Section III presents our theoretical analysis regarding the influence of the source correlation on the adaptive beamformer performance. Section IV presents the results of several numerical experiments that validate the arguments in Section III. Throughout this paper, plain italics indicate scalars, lower case boldface italics indicate vectors, and upper case boldface italics indicate matrices.

Manuscript received January 8, 2002; revised July 15, 2002. This work was supported by Grants-in-Aid from the Kayamori Foundation of Informational Science Advancement, Grants-in-Aid from the Suzuki Foundation, and Grants-in-Aid from the Ministry of Education, Science, Culture and Sports in Japan (C13680948). This work was also supported in part by the Whitaker Foundation and by National Institute of Health (R01-DC004855-01). *Asterisk indicates corresponding author.*

*K. Sekihara is with the Department of Electronic Systems and Engineering, Tokyo Metropolitan Institute of Technology, Tokyo 191-0065, Japan (e-mail: ksekiha@cc.tmit.ac.jp).

S. S. Nagarajan was with the Department of Bioengineering, University of Utah, Salt Lake City, UT 84112-9202 USA. He is now with the Department of Radiology, the University of California, San Francisco, CA 94143 USA.

D. Poeppel is with the Department of Linguistics and Biology, University of Maryland, College Park, MD 20742 USA.

A. Marantz is with the Department of Linguistics and Philosophy, Massachusetts Institute of Technology, Cambridge, MA 02139 USA.

Digital Object Identifier 10.1109/TBME.2002.805485

II. Adaptive-Beamformer Techniques for Neuromegnetic Reconstruction

A. Definitions

We define the magnetic field measured by the mth detector coil at time t as $b_m(t)$, and a column vector $\boldsymbol{b}(t) = [b_1(t), b_2(t), \ldots, b_M(t)]^T$ as a set of measured data where M is the total number of detector coils and superscript T indicates the matrix transpose. The spatial location is represented by a three-dimensional (3-D) vector $\boldsymbol{r}$: $\boldsymbol{r} = (x, y, z)$. A total of Q discrete sources are assumed to generate the neuromagnetic field. These discrete sources are modeled using the equivalent current dipoles [17]. The number of sources Q is assumed to be less than the number of sensors M; i.e., the measured neuromagnetic signal is assumed to be a low-rank signal [18], [19]. The locations of these sources are denoted as $\boldsymbol{r}_1, \boldsymbol{r}_2, \ldots, \boldsymbol{r}_Q$. The moment magnitude of the qth source at time t is denoted as $s(\boldsymbol{r}_q, t)$, and the source magnitude vector is defined as $\boldsymbol{s}(t) = [s(\boldsymbol{r}_1, t), s(\boldsymbol{r}_2, t), \ldots, s(\boldsymbol{r}_Q, t)]^T$.

The orientation of the qth source is defined as a 3-D column vector $\boldsymbol{\eta}(\boldsymbol{r}_q, t) = [\eta_x(\boldsymbol{r}_q, t), \eta_y(\boldsymbol{r}_q, t), \eta_z(\boldsymbol{r}_q, t)]^T$ whose ζ component (where ζ equals x, y, or z in this paper) is equal to the cosine of the angle between the direction of the source moment and the ζ direction. We assume that the orientation of each source is time independent. Omitting time notation t, we define a $3Q \times Q$ matrix that expresses the orientations of all Q sources as $\boldsymbol{\Psi}$ such that

$$\boldsymbol{\Psi} = \begin{bmatrix} \boldsymbol{\eta}(\boldsymbol{r}_1) & 0 & \cdots & 0 \\ 0 & \boldsymbol{\eta}(\boldsymbol{r}_2) & \cdot & \vdots \\ \vdots & \cdot & \ddots & 0 \\ 0 & \cdots & 0 & \boldsymbol{\eta}(\boldsymbol{r}_Q) \end{bmatrix}.$$

We define $l_m^{\zeta}(\boldsymbol{r})$ as the output of the mth sensor; the output is induced by the unit-magnitude source located at $\boldsymbol{r}$ and directed in the ζ direction. The column vector $\boldsymbol{l}_{\zeta}(\boldsymbol{r})$ is defined as $\boldsymbol{l}_{\zeta}(\boldsymbol{r}) = [l_1^{\zeta}(\boldsymbol{r}), l_2^{\zeta}(\boldsymbol{r}), \ldots, l_M^{\zeta}(\boldsymbol{r})]^T$. Next, the lead field matrix, which represents the sensitivity of the whole sensor array at $\boldsymbol{r}$, is defined as $\boldsymbol{L}(\boldsymbol{r}) = [\boldsymbol{l}_x(\boldsymbol{r}), \boldsymbol{l}_y(\boldsymbol{r}), \boldsymbol{l}_z(\boldsymbol{r})]$. The lead-field vector in the source-moment direction is defined, for later use, as $\boldsymbol{l}(\boldsymbol{r})$ where $\boldsymbol{l}(\boldsymbol{r}) = \boldsymbol{L}(\boldsymbol{r})\boldsymbol{\eta}(\boldsymbol{r})$. The composite lead field matrix for the entire set of Q sources is defined as

$$\boldsymbol{L}_c = [\boldsymbol{L}(\boldsymbol{r}_1), \boldsymbol{L}(\boldsymbol{r}_2), \ldots, \boldsymbol{L}(\boldsymbol{r}_Q)]. \tag{1}$$

The relationship between $\boldsymbol{b}(t)$ and $\boldsymbol{s}(t)$ is then expressed as

$$\boldsymbol{b}(t) = (\boldsymbol{L}_c\boldsymbol{\Psi})\boldsymbol{s}(t) + \boldsymbol{n}(t) \tag{2}$$

where $\boldsymbol{n}(t)$ is the additive noise. Defining $\overline{\boldsymbol{L}}_c$ as $\overline{\boldsymbol{L}}_c = \boldsymbol{L}_c\boldsymbol{\Psi}$, this relationship is rewritten as

$$\boldsymbol{b}(t) = \overline{\boldsymbol{L}}_c\boldsymbol{s}(t) + \boldsymbol{n}(t) \tag{3}$$

where

$$\begin{aligned} \overline{\boldsymbol{L}}_c &= [\boldsymbol{L}(\boldsymbol{r}_1)\boldsymbol{\eta}(\boldsymbol{r}_1), \boldsymbol{L}(\boldsymbol{r}_2)\boldsymbol{\eta}(\boldsymbol{r}_2), \ldots, \boldsymbol{L}(\boldsymbol{r}_Q)\boldsymbol{\eta}(\boldsymbol{r}_Q)] \\ &= [\boldsymbol{l}(\boldsymbol{r}_1), \boldsymbol{l}(\boldsymbol{r}_2), \ldots, \boldsymbol{l}(\boldsymbol{r}_Q)]. \end{aligned} \tag{4}$$

The matrix $\overline{\boldsymbol{L}}_c$ is the composite lead field matrix whose column is equal to the lead field vector in the source-moment direction. The measurement covariance matrix is denoted as $\boldsymbol{R}_b$, which is obtained from $\boldsymbol{R}_b = \langle \boldsymbol{b}(t)\boldsymbol{b}^T(t) \rangle$, where $\langle \cdot \rangle$ indicates the ensemble average, which is replaced with the time average over a certain time window in practice. It should be noted that when $\langle \boldsymbol{b}(t) \rangle$ is not equal to zero, $\boldsymbol{R}_b$ is not equal to the covariance matrix and should rather be referred to as the second-order moment matrix in such a case. However, according to convention, $\boldsymbol{R}_b$ is referred to as a covariance matrix in this paper. The covariance matrix of the source-moment activity is defined here as $\boldsymbol{R}_s$; i.e., $\boldsymbol{R}_s = \langle \boldsymbol{s}(t)\boldsymbol{s}^T(t) \rangle$.

Using (3) and assuming that the noise $\boldsymbol{n}(t)$ and the source activity $\boldsymbol{s}(t)$ are uncorrelated, we get the relationship between the measurement covariance matrix and the source-activity covariance matrix such that

$$\boldsymbol{R}_b = \overline{\boldsymbol{L}}_c\boldsymbol{R}_s\overline{\boldsymbol{L}}_c^T + \sigma^2\boldsymbol{I} \tag{5}$$

where the noise in the measured data is assumed to be the white Gaussian noise with a variance of σ^2 and $\boldsymbol{I}$ is the identity matrix. The jth eigenvalue and the eigenvector of $\boldsymbol{R}_b$ are defined as λ_j and $\boldsymbol{e}_j$, respectively. Unless some source activities are perfectly correlated with each other, the rank of $\boldsymbol{R}_s$ is equal to the number of sources Q. Therefore, according to (5), $\boldsymbol{R}_b$ has Q eigenvalues greater than σ^2 and $M-Q$ eigenvalues equal to σ^2. For later use, the matrix $\boldsymbol{E}_S$ is defined as $\boldsymbol{E}_S = [\boldsymbol{e}_1, \ldots, \boldsymbol{e}_Q]$. The column span of $\boldsymbol{E}_S$ is the maximum-likelihood estimate of the signal subspace of $\boldsymbol{R}_b$ [20].

It should be pointed out that, in (5), interference magnetic fields originated from external noise sources such as brain background activities can be considered as a part of signals, and their influence can be accounted for in the first term of the right-hand side of this equation. The noise here indicates only noises with internal origins, such as those originated from the sensor coils, the superconducting quamtum interference devices (SQUIDs), and their associated electronics. Therefore, the assumption of spatially uncorrelated white Gaussian noise is acceptable for deriving (5).

B. Scalar Minimum-Variance Beamformer

To estimate the source moment, we have focused on the class of techniques referred to as the adaptive beamformer [21]. This type of technique uses the following spatial-filter operation for estimating the source moment:

$$\tilde{s}(\boldsymbol{r}, t) = \boldsymbol{w}^T(\boldsymbol{r})\boldsymbol{b}(t) \tag{6}$$

where $\tilde{s}(\boldsymbol{r}, t)$ is the source-moment time course obtained as the beamformer output. One well-known adaptive beamformer is the minimum-variance distortion-less beamformer originally developed in the field of array signal processing [22]. This technique derives the weight vector $\boldsymbol{w}(\boldsymbol{r})$ by minimizing $\boldsymbol{w}^T(\boldsymbol{r})\boldsymbol{R}_b\boldsymbol{w}(\boldsymbol{r})$ under the constraint of $\boldsymbol{l}^T(\boldsymbol{r})\boldsymbol{w}(\boldsymbol{r}) = 1$. The explicit form of the weight vector for the minimum-variance beamformer is known to be

$$\boldsymbol{w}(\boldsymbol{r}) = \frac{\boldsymbol{R}_b^{-1}\boldsymbol{l}(\boldsymbol{r})}{\boldsymbol{l}^T(\boldsymbol{r})\boldsymbol{R}_b^{-1}\boldsymbol{l}(\boldsymbol{r})}. \tag{7}$$

Note that to use this formula, the source orientation $\boldsymbol{\eta}(\boldsymbol{r})$ is needed to calculate $\boldsymbol{l}(\boldsymbol{r})$. However, $\boldsymbol{\eta}(\boldsymbol{r})$ is generally unknown,

although several techniques have been developed to estimate it [12], [23].

C. Vector Minimum-Variance Beamformer Formulation

A vector-type beamformer uses a set of three weight vectors, $\boldsymbol{w}_x(\boldsymbol{r})$, $\boldsymbol{w}_y(\boldsymbol{r})$, and $\boldsymbol{w}_z(\boldsymbol{r})$, each of which estimates the x, y, and z components of the source moment, thus enabling the source orientation as well as the source-moment magnitude to be estimated. A set of weight vectors for a vector-extended minimum-variance beamformer is given by [24], [25]

$$[\boldsymbol{w}_x(\boldsymbol{r}),\, \boldsymbol{w}_y(\boldsymbol{r}),\, \boldsymbol{w}_z(\boldsymbol{r})] = \boldsymbol{R}_b^{-1}\boldsymbol{L}(\boldsymbol{r})[\boldsymbol{L}^T(\boldsymbol{r})\boldsymbol{R}_b^{-1}\boldsymbol{L}(\boldsymbol{r})]^{-1}. \quad (8)$$

Using these weight vectors, the x, y, and z components of the source moment are given by

$$[\tilde{s}_x(\boldsymbol{r},\, t),\, \tilde{s}_y(\boldsymbol{r},\, t),\, \tilde{s}_z(\boldsymbol{r},\, t)]^T = [\boldsymbol{w}_x^T(\boldsymbol{r}),\, \boldsymbol{w}_y^T(\boldsymbol{r}),\, \boldsymbol{w}_z^T(\boldsymbol{r})]^T\boldsymbol{b}(t) \quad (9)$$

where $\tilde{s}_\zeta(\boldsymbol{r},\, t)$ is the estimated source moment in the ζ direction. The estimate of the source-moment orientation is denoted as $[\hat{\eta}_x,\, \hat{\eta}_y,\, \hat{\eta}_z]$, which can be extracted from (9) such that

$$[\hat{\eta}_x,\, \hat{\eta}_y,\, \hat{\eta}_z]^T = [\boldsymbol{w}_x^T(\boldsymbol{r}),\, \boldsymbol{w}_y^T(\boldsymbol{r}),\, \boldsymbol{w}_z^T(\boldsymbol{r})]^T\boldsymbol{b}(t) \Big/ \left\|[\boldsymbol{w}_x^T(\boldsymbol{r}),\, \boldsymbol{w}_y^T(\boldsymbol{r}),\, \boldsymbol{w}_z^T(\boldsymbol{r})]^T\boldsymbol{b}(t)\right\|. \quad (10)$$

The magnitude of the source moment is estimated from

$$\tilde{s}(\boldsymbol{r},\, t) = \boldsymbol{w}_V^T(\boldsymbol{r})\boldsymbol{b}(t) \quad (11)$$

where $\boldsymbol{w}_V(\boldsymbol{r}) = [\hat{\eta}_x\boldsymbol{w}_x(\boldsymbol{r}) + \hat{\eta}_y\boldsymbol{w}_y(\boldsymbol{r}) + \hat{\eta}_z\boldsymbol{w}_z(\boldsymbol{r})]$. It can be seen that the composite weight vector $\boldsymbol{w}_V(\boldsymbol{r})$ is equivalent to the weight vector for the scalar beamformer $\boldsymbol{w}(\boldsymbol{r})$ in (7). In the following analysis, we use $\boldsymbol{w}(\boldsymbol{r})$ for simplicity, but the results of the analysis are also valid for $\boldsymbol{w}_V(\boldsymbol{r})$.

D. Eigenspace-Projected Beamformer

The minimum-variance beamformer is known to be very sensitive to errors in the forward modeling or errors in estimating the measurement covariance matrix. In the case of neuromagnetic measurements, since such errors are almost inevitable, the minimum-variance beamformer generally provides noisy results. The eigenspace-projection beamformer provides an output signal-to-noise ratio (SNR) much higher than that of the minimum-variance beamformer when such errors mentioned above exist [26]. The extension of the minimum-variance beamformer to the eigenspace-projection beamformer is attained by projecting the weight vector of the minimum-variance beamformer onto the signal subspace of the measurement covariance matrix. That is, redefining the weight vector obtained from (7) as $\boldsymbol{w}^{(\mathrm{MV})}$, the eigenspace-projection beamformer is given by [26]

$$\boldsymbol{w}(\boldsymbol{r}) = \boldsymbol{E}_S\boldsymbol{E}_S^T\boldsymbol{w}^{(\mathrm{MV})}(\boldsymbol{r}) \quad (12)$$

or redefining the weight vectors obtained from (8) as $[\boldsymbol{w}_x^{(\mathrm{MV})},\, \boldsymbol{w}_y^{(\mathrm{MV})},\, \boldsymbol{w}_z^{(\mathrm{MV})}]$, the vector-extended eigenspace beamformer is given by [7]

$$[\boldsymbol{w}_x(\boldsymbol{r}),\, \boldsymbol{w}_y(\boldsymbol{r}),\, \boldsymbol{w}_z(\boldsymbol{r})] = \boldsymbol{E}_S\boldsymbol{E}_S^T\left[\boldsymbol{w}_x^{(\mathrm{MV})}(\boldsymbol{r}),\, \boldsymbol{w}_y^{(\mathrm{MV})}(\boldsymbol{r}),\, \boldsymbol{w}_z^{(\mathrm{MV})}(\boldsymbol{r})\right]. \quad (13)$$

III. Beamformer Performance When Sources are Correlated

A. Signal Leakage and Errors in Time-Course Estimate

The weight vector for the minimum-variance beamformer is obtained by minimizing the output power $\tilde{P}$; $\tilde{P} = \boldsymbol{w}^T(\boldsymbol{r})\boldsymbol{R}_b\boldsymbol{w}(\boldsymbol{r})$ under the constraint $\boldsymbol{w}^T(\boldsymbol{r})\boldsymbol{l}(\boldsymbol{r}) = 1$. When the beamformer pointing location $\boldsymbol{r}$ is equal to the source location $\boldsymbol{r}_p$, neglecting the noise term, the output power is rewritten as

$$\begin{aligned}\tilde{P} &= \left\langle \left\| \boldsymbol{w}^T(\boldsymbol{r}_p)\sum_{q=1}^{Q}\boldsymbol{l}(\boldsymbol{r}_q)s(\boldsymbol{r}_q,\, t)\right\|^2\right\rangle \\ &= \sum_{q=1}^{Q}\left\langle s(\boldsymbol{r}_q,\, t)^2\right\rangle \|\boldsymbol{w}^T(\boldsymbol{r}_p)\boldsymbol{l}(\boldsymbol{r}_q)\|^2 \\ &= \left\langle s(\boldsymbol{r}_p,\, t)^2\right\rangle + \sum_{q\neq p}\left\langle s(\boldsymbol{r}_q,\, t)^2\right\rangle \|\boldsymbol{w}^T(\boldsymbol{r}_p)\boldsymbol{l}(\boldsymbol{r}_q)\|^2 \end{aligned} \quad (14)$$

where sources are assumed to be uncorrelated with each other, and the relationship $\boldsymbol{w}^T(\boldsymbol{r}_p)\boldsymbol{l}(\boldsymbol{r}_p) = 1$ is used. Thus, the weight vector obtained by minimizing $\tilde{P}$ should have the property that $\boldsymbol{w}^T(\boldsymbol{r}_p)\boldsymbol{l}(\boldsymbol{r}_q) = 0$ where $p \neq q$. That is, the resultant weight should only pass the signal from $\boldsymbol{r}_p$, and block the signal from other sources, and the blocking capability of the beamformer weight is expressed as

$$\boldsymbol{w}^T(\boldsymbol{r}_p)\boldsymbol{l}(\boldsymbol{r}_q) = \delta_{p,\,q} \quad (15)$$

where $\delta_{p,\,q}$ is the Kronecker delta defined as $\delta_{p,\,q} = 1$ $(p = q)$ and $\delta_{p,\,q} = 0$ $(p \neq q)$.

In general cases where partially correlated sources exist, however, the blocking capability of the weight vector is expressed in the following equation:

$$\boldsymbol{w}^T(\boldsymbol{r}_p)\boldsymbol{l}(\boldsymbol{r}_q) = \frac{[\boldsymbol{R}_s^{-1}]_{pq}}{[\boldsymbol{R}_s^{-1}]_{pp}} \quad (16)$$

where $[\boldsymbol{R}_s^{-1}]_{pq}$ indicates the $(p,\, q)$ element of $\boldsymbol{R}_s^{-1}$. This equation, first derived by Zoltowski [27], is the basis of our analysis. Its derivation is described in Appendix I and, as shown in this derivation, (16) exactly holds when the SNR is so high that noise can be neglected. We assume that the target source exists at $\boldsymbol{r}_p$ and that the Q_I sources are correlated with the target source. (A total of $Q_I + 1$ sources are mutually correlated). The beamformer output at $\boldsymbol{r}_p$, $\tilde{s}(\boldsymbol{r}_p,\, t)$, is expressed as

$$\tilde{s}(\boldsymbol{r}_p,\, t) = s(\boldsymbol{r}_p,\, t) + \sum_{q=1}^{Q_I}\frac{[\boldsymbol{R}_s^{-1}]_{pq}}{[\boldsymbol{R}_s^{-1}]_{pp}}\, s(\boldsymbol{r}_q,\, t) \quad (17)$$

where the locations of the correlated interferences are denoted as $\boldsymbol{r}_q$, $(q = 1,\, \ldots,\, Q_I)$. This equation shows that the beamformer outputs for the correlated sources contain leakage from the other correlated sources, and such leakage causes errors in the time-course estimates of the source activities.

We consider a case where, among Q sources, the first and the second sources are significantly correlated and the other sources have no significant correlation with any other sources. We define the correlation coefficient between the first and the second sources as μ, and the average power of the jth source as α_j^2,

TABLE I
SOURCE PARAMETER VALUES USED FOR THE NUMERICAL EXPERIMENTS IN SECTION IV

source number	location (cm)	orientation
1	(1.0, −1.0, −6.0)	(1.0, 0., 0.)
2	(1.0, 1.0, −6.0)	(0.7, 0.7, 0.)
3	(1.0, 1.6, −7.2)	(0, 0.7, 0.7)

where $\alpha_j^2 = \langle s(\boldsymbol{r}_j, t)^2 \rangle$. The source covariance matrix and its inverse can be expressed as in (18) and (19), shown at the bottom of the page.

Using (16) and (19), we can derive

$$\boldsymbol{w}(\boldsymbol{r}_1)\boldsymbol{l}(\boldsymbol{r}_1) = 1 \quad \boldsymbol{w}(\boldsymbol{r}_1)\boldsymbol{l}(\boldsymbol{r}_2) = -\frac{\alpha_1}{\alpha_2}\mu$$
$$\boldsymbol{w}(\boldsymbol{r}_2)\boldsymbol{l}(\boldsymbol{r}_2) = -\frac{\alpha_2}{\alpha_1}\mu \quad \boldsymbol{w}(\boldsymbol{r}_2)\boldsymbol{l}(\boldsymbol{r}_2) = 1 \tag{20}$$

and

$$\boldsymbol{w}(\boldsymbol{r}_1)\boldsymbol{l}(\boldsymbol{r}_j) = 0 \quad \boldsymbol{w}(\boldsymbol{r}_2)\boldsymbol{l}(\boldsymbol{r}_j) = 0 \quad \text{for } j = 3, \ldots, Q. \tag{21}$$

Therefore, when the beamformer is pointing at the first source location $\boldsymbol{r}_1$, it passes the signal from the second source with the multiplicative constant of $-\alpha_1\mu/\alpha_2$, although it blocks the signals from the other sources uncorrelated with the first source. Consequently, the beamformer output at $\boldsymbol{r}_1$, $\tilde{s}(\boldsymbol{r}_1, t)$, is given by

$$\tilde{s}(\boldsymbol{r}_1, t) = s(\boldsymbol{r}_1, t) - \left(\frac{\alpha_1}{\alpha_2}\mu\right) s(\boldsymbol{r}_2, t). \tag{22}$$

In exactly the same manner, the beamformer output at $\boldsymbol{r}_2$, $\tilde{s}(\boldsymbol{r}_2, t)$, is given by

$$\tilde{s}(\boldsymbol{r}_2, t) = s(\boldsymbol{r}_2, t) - \left(\frac{\alpha_2}{\alpha_1}\mu\right) s(\boldsymbol{r}_1, t). \tag{23}$$

These equations explicitly show that the beamformer output for the first source contains the leakage from the second source and that the output for the second source contains the leakage from the first source. Equations (22) and (23) are valid for high SNR, but they still hold for considerably low SNR, as is shown in our numerical experiments.

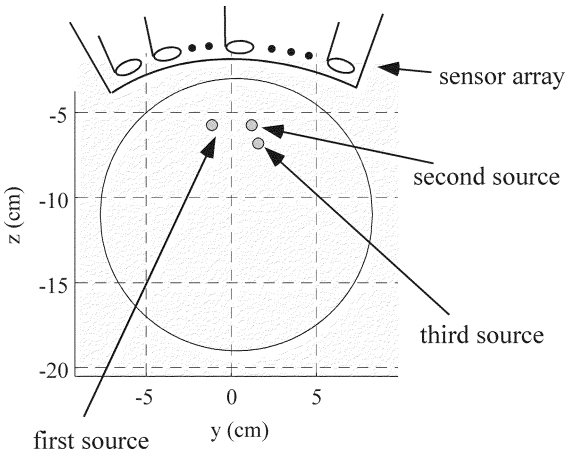

Fig. 1. The coordinate system and source-detector configuration used in the numerical experiments. The coordinate origin was set at the center of the detector coil located at the center of the coil array. The plane at $x = 1.0$ cm is shown. The large circle shows the cross section of the sphere used for the forward calculation.

TABLE II
VALUES OF THE PARAMETERS USED FOR CALCULATING $w_1(t)$, $w_2(t)$, AND $w_3(t)$

$w_j(t)$ (ms)	Ω (ms)	t_1 (ms)	f (1/ms)	t_θ (ms)
$j = 1$	67.8	219	0.0095	139
$j = 2$	105.3	246	0.0158	123
$j = 3$	–	–	0.0228	100

B. Signal-Intensity Reduction and Correlation-Coefficient Estimation

The leakage from correlated activities not only causes errors in the time-course estimate but also causes intensity reduction

$$\boldsymbol{R}_s = \begin{bmatrix} \begin{bmatrix} \alpha_1^2 & \mu\alpha_1\alpha_2 \\ \mu\alpha_1\alpha_2 & \alpha_2^2 \end{bmatrix} & 0 & \cdots & 0 \\ 0 & \alpha_3^2 & \cdot & \vdots \\ \vdots & \cdot & \ddots & 0 \\ 0 & \cdots & 0 & \alpha_Q^2 \end{bmatrix} \tag{18}$$

and

$$\boldsymbol{R}_s^{-1} = \begin{bmatrix} \dfrac{1}{\alpha_1^2\alpha_2^2(1-\mu^2)} \begin{bmatrix} \alpha_2^2 & -\mu\alpha_1\alpha_2 \\ -\mu\alpha_1\alpha_2 & \alpha_1^2 \end{bmatrix} & 0 & \cdots & 0 \\ 0 & 1/\alpha_3^2 & \cdot & \vdots \\ \vdots & \cdot & \ddots & 0 \\ 0 & \cdots & 0 & 1/\alpha_Q^2 \end{bmatrix}. \tag{19}$$

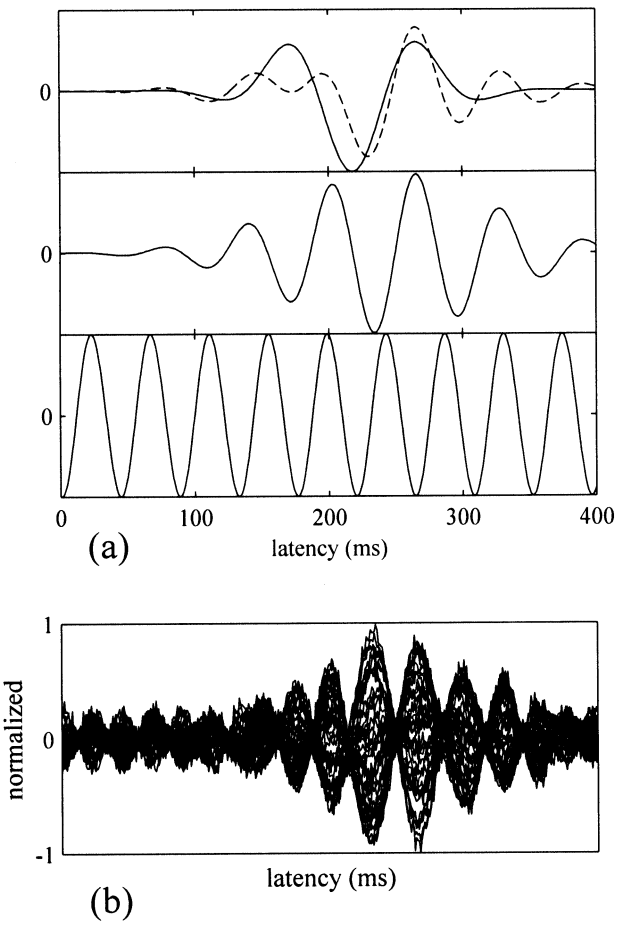

Fig. 2. (a) Time courses $w_1(t)$, $w_2(t)$, and $w_3(t)$ used for the numerical experiments. The top panel represents $w_1(t)$, the middle one, $w_2(t)$, and the bottom one, $w_3(t)$. Each time course is normalized by its maximum value. The broken line in the top panel indicates time course $w_1'(t)$, which is obtained from $w_1'(t) = (1-\xi)w_1(t) + \xi w_2(t)$ with $\xi = 0.5$. The correlation coefficient between $w_1'(t)$ and $w_2(t)$, μ, is 0.8 in this case. (b) Examples of the simulated magnetic-field recordings when SNR is equal to four and $\xi = 0$.

in the reconstructed source activities. Using (22) and (23) with the relationship $\langle s(\boldsymbol{r}_1, t)s(\boldsymbol{r}_2, t)\rangle = \mu\alpha_1\alpha_2$, we get

$$\langle \tilde{s}(\boldsymbol{r}_1, t)\tilde{s}(\boldsymbol{r}_2, t)\rangle = \alpha_1\alpha_2(\mu^3 - \mu) \tag{24}$$

$$\langle \tilde{s}(\boldsymbol{r}_1, t)^2\rangle = \alpha_1^2(1-\mu^2) \tag{25}$$

and

$$\langle \tilde{s}(\boldsymbol{r}_2, t)^2\rangle = \alpha_2^2(1-\mu^2). \tag{26}$$

Equations (25) and (26) indicate that the power of the reconstructed sources is reduced by a factor of $1-\mu^2$. This reduction of source power has been known as the signal cancellation in the field of the array signal processing [28], [29].

We define the magnitude correlation coefficient between the first and the second sources calculated from the beamformer output $\tilde{\mu}$ as

$$\tilde{\mu} = \frac{|\langle \tilde{s}(\boldsymbol{r}_1, t)\tilde{s}(\boldsymbol{r}_2, t)\rangle|}{\sqrt{\langle \tilde{s}(\boldsymbol{r}_1, t)^2\rangle \langle \tilde{s}(\boldsymbol{r}_2, t)^2\rangle}}. \tag{27}$$

Substituting (24)–(26) into (27), we finally obtain

$$\tilde{\mu} = \frac{|\alpha_1\alpha_2(\mu^3 - \mu)|}{\sqrt{\alpha_1^2(1-\mu^2)\alpha_2^2(1-\mu^2)}} = |\mu|. \tag{28}$$

This equation indicates that the magnitude correlation coefficient can be accurately estimated by substituting the beamformer outputs into (27). Appendix II shows that the magnitude of the cross coherence in the frequency domain can also be correctly estimated by using the outputs from the frequency-domain beamformer.

If a third correlated source exists, the accuracy of the estimated correlation coefficient should be affected by this source. This influence can be evaluated in the following manner. We assume that the first, second, and third sources are mutually correlated, and their correlation coefficients are denoted as μ_{12}, μ_{13}, and μ_{23}. We further assume that the correlation between the first and second sources is the target of the measurement and the third source is an interference. According to (17), the beamformer outputs at the target source locations are

$$\tilde{s}(\boldsymbol{r}_1, t) = \frac{1}{\left[\overline{\boldsymbol{R}}_s^{-1}\right]_{11}}\left\{\left[\overline{\boldsymbol{R}}_s^{-1}\right]_{11} s(\boldsymbol{r}_1, t) + \left[\overline{\boldsymbol{R}}_s^{-1}\right]_{12} s(\boldsymbol{r}_2, t) + \left[\overline{\boldsymbol{R}}_s^{-1}\right]_{13} s(\boldsymbol{r}_3, t)\right\} \tag{29}$$

and

$$\tilde{s}(\boldsymbol{r}_2, t) = \frac{1}{\left[\overline{\boldsymbol{R}}_s^{-1}\right]_{22}}\left\{\left[\overline{\boldsymbol{R}}_s^{-1}\right]_{21} s(\boldsymbol{r}_1, t) + \left[\overline{\boldsymbol{R}}_s^{-1}\right]_{22} s(\boldsymbol{r}_2, t) + \left[\overline{\boldsymbol{R}}_s^{-1}\right]_{23} s(\boldsymbol{r}_3, t)\right\} \tag{30}$$

where $\boldsymbol{r}_3$ is the location of the third source, and $\overline{\boldsymbol{R}}_s$ is the source-covariance submatrix related to the correlated three sources. (This $\overline{\boldsymbol{R}}_s$ is presented in Appendix III.)

Using (27), (29), (30), and (45), we finally obtain

$$\tilde{\mu}_{12} = \frac{|\mu_{12} - \mu_{13}\mu_{23}|}{\sqrt{(1-\mu_{13}^2)(1-\mu_{23}^2)}}. \tag{31}$$

This equation shows how the values of μ_{13} and μ_{23} affect $\tilde{\mu}_{12}$. Clearly, when μ_{13} and μ_{23} are small, $\tilde{\mu}_{12}$ is close to $|\mu_{12}|$.

C. Retrieval of Original Time Courses

As discussed in the preceding sections, the beamformer output $\tilde{s}(\boldsymbol{r}_j, t)$ contains not only the target source activities but also the activities correlated with the target sources. However, if we know the amount of correlated interference contained in $\tilde{s}(\boldsymbol{r}_j, t)$, the original target-source time courses can be retrieved by inverting (22) and (23), i.e.,

$$\begin{bmatrix}\hat{s}(\boldsymbol{r}_1, t)\\ \hat{s}(\boldsymbol{r}_2, t)\end{bmatrix} = \begin{bmatrix}1 & -(\alpha_1/\alpha_2)\mu\\ -(\alpha_2/\alpha_1)\mu & 1\end{bmatrix}^{-1}\begin{bmatrix}\tilde{s}(\boldsymbol{r}_1, t)\\ \tilde{s}(\boldsymbol{r}_2, t)\end{bmatrix} \tag{32}$$

where $\hat{s}(\boldsymbol{r}_j, t)$ is the retrieved time course of the jth source where $j = 1$ and 2. In the right-hand side of the aforementioned equation, μ can be estimated from (28), and α_1 and α_2 can be obtained from $\alpha_1^2 = \langle \tilde{s}(\boldsymbol{r}_1, t)^2\rangle/(1-\mu^2)$ and $\alpha_2^2 = \langle \tilde{s}(\boldsymbol{r}_2, t)^2\rangle/(1-\mu^2)$.

IV. Numerical Experiments

A. Data Generation

A series of numerical experiments were conducted to verify the validity of the arguments presented in Section III. In particular, we have shown that the arguments still hold even for

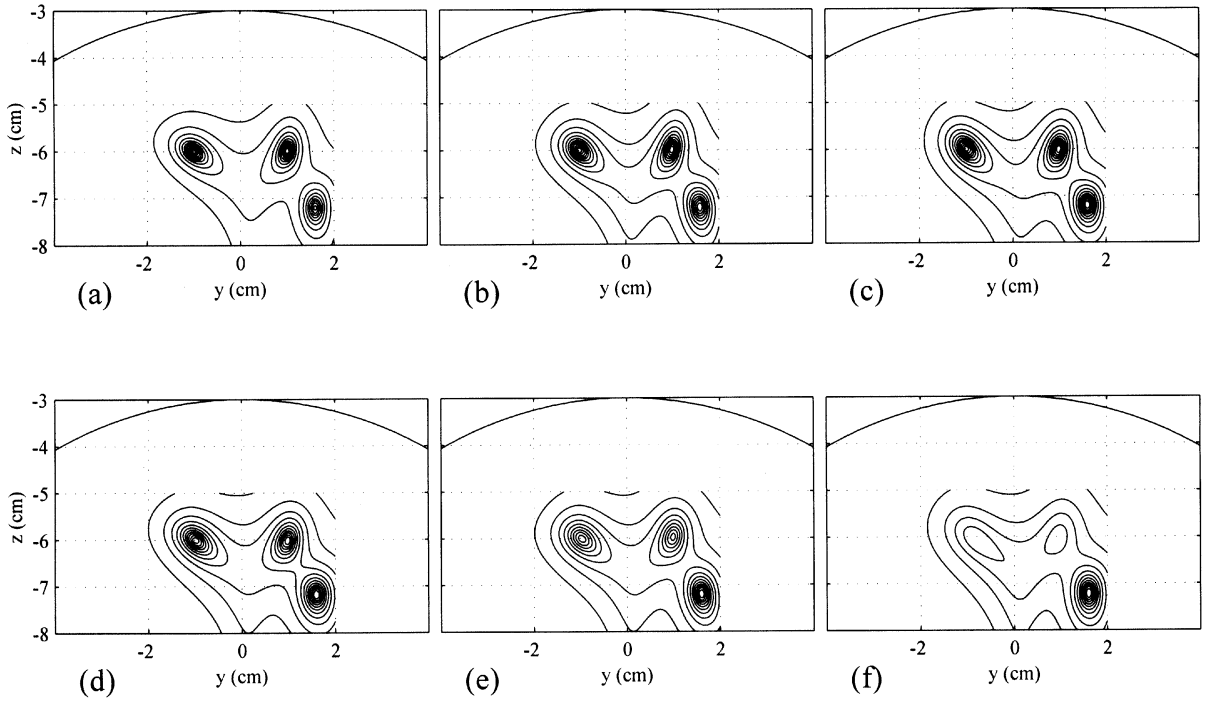

Fig. 3. Magnitude-squared average reconstruction $\sqrt{\langle \bar{s}(\boldsymbol{r}, t)^2 \rangle}$ obtained by using the minimum-variance beamformer in (8) and (11). SNR is equal to 16. (a) $\mu = 0.08$. (b) $\mu = 0.5$. (c) $\mu = 0.6$. (d) $\mu = 0.7$. (e) $\mu = 0.8$. (f) $\mu = 0.95$. μ is the cross-correlation coefficient between the first and second sources.

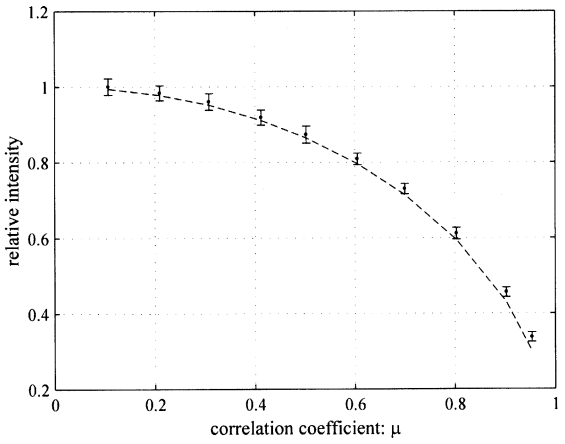

Fig. 4. Intensity of the first source with respect to the correlation between the first and second sources. The broken line indicates the theoretical relationship $\sqrt{1-\mu^2}$. In these Monte Carlo simulations, the mean intensity of the first source was calculated from 100 generated data sets. The error bars indicate the range of ± 2 standard deviations. The SNR was set to four.

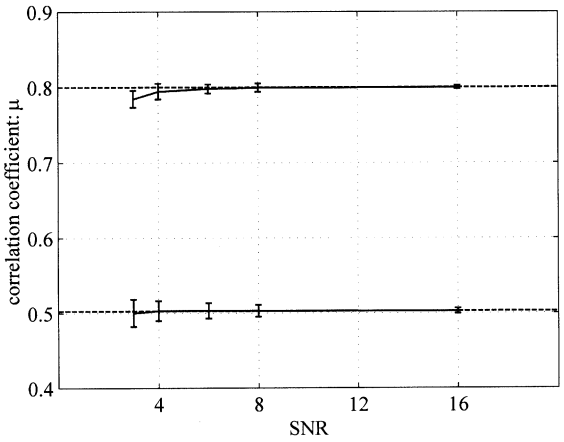

Fig. 5. Estimated correlation coefficient between the first and second sources. Monte Carlo-type simulations, which generated 100 sets of magnetic recordings, were performed and the average values of $\bar{\mu}$ for five SNRs are plotted. The error bar shows the ± 2 standard deviations. The experiments were repeated for $\mu = 0.8$ and $\mu = 0.5$. The broken horizontal lines show the true values of the correlation coefficient.

low-SNR cases, although the arguments are based on the assumption that noise can be neglected. A sensor alignment of the 37-sensor array from Magnes[1] neuromagnetometer was used in which the sensor coils are arranged in a uniform, concentric array on a spherical surface with a radius of 12.2 cm. The sensors are first-order axial gradiometers with a baseline of 5 cm. The coordinate origin was set at the center of the detector coil located at the center of the coil array. The x direction was defined as that from the posterior to the anterior, and the y direction was defined as that from the right to the left hemispheres. Three point sources were assumed to exist on a plane defined as $x = 1.0$. [The values of the spatial coordinates (x, y, z) are expressed in centimeters.] The locations as well as the orientations of the sources are listed in Table I. The source-sensor configuration and the coordinate system are illustrated in Fig. 1.

First, three time courses $w_1(t)$, $w_2(t)$, and $w_3(t)$ were calculated by using

$$w_j(t) = \exp\left[(t-t_1)^2/\Omega^2\right] \sin[2\pi f(t-t_\theta)] \quad \text{for } j = 1, 2 \tag{33}$$

and

$$w_3(t) = \sin[2\pi f(t-t_\theta)] \tag{34}$$

[1]4D Neuroimaging Inc., San Diego, CA

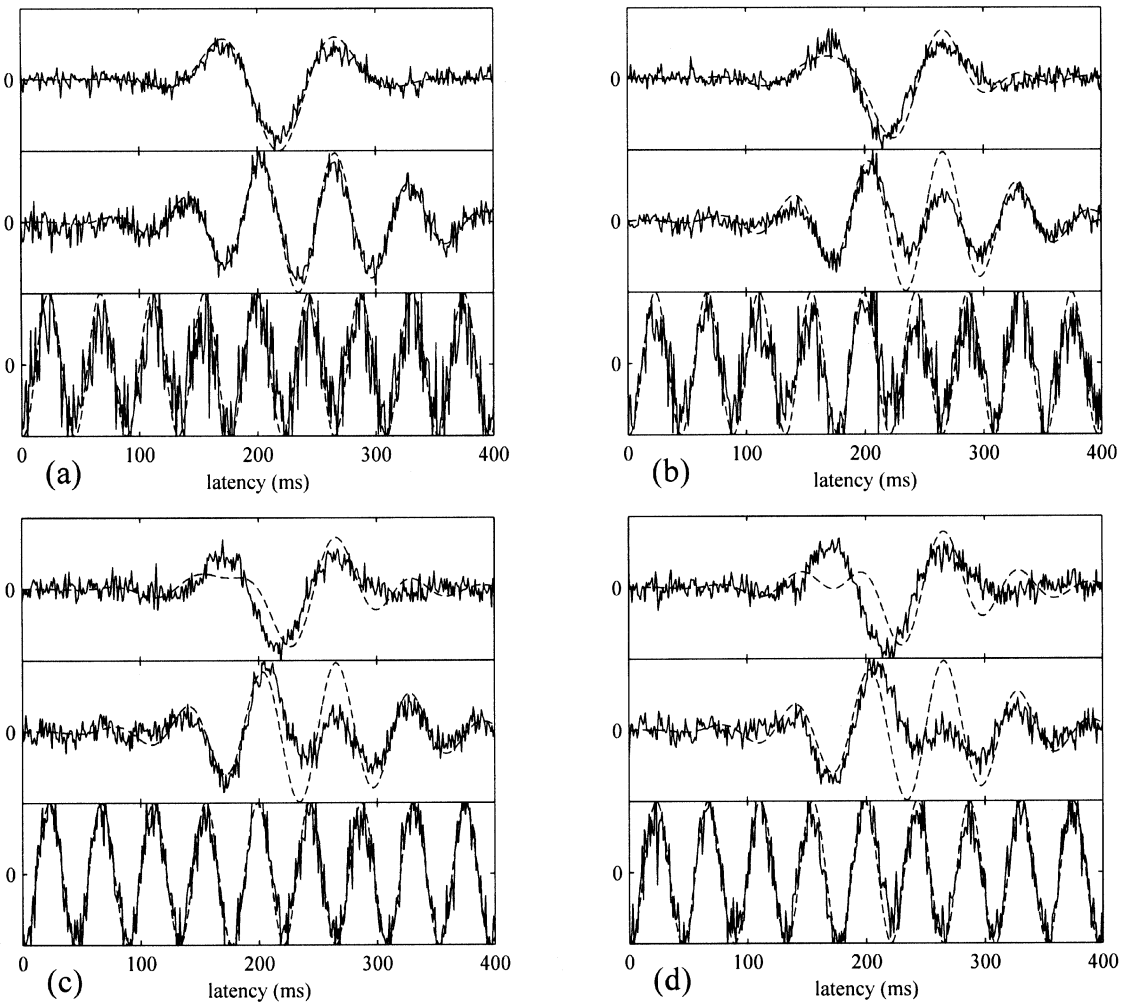

Fig. 6. Time-course outputs obtained by using the minimum-variance beamformer for the three sources when SNR is equal to four and (a) $\mu = 0.08$, (b) $\mu = 0.4$, (c) $\mu = 0.6$, and (d) $\mu = 0.8$. Time courses from the first to third sources are shown from top to bottom. The solid lines indicate the beamformer outputs and the broken lines indicate the original time courses.

where Ω, t_1, f, and t_θ are the numerical parameters controlling the shapes of the time courses. The values of these parameters used in these experiments are listed in Table II. Time courses $w_1(t)$, $w_2(t)$, and $w_3(t)$, are shown by the solid lines in Fig. 2(a). The correlation coefficients of these three time courses are 8×10^{-2} between $w_1(t)$ and $w_2(t)$, 2×10^{-4} between $w_1(t)$ and $w_3(t)$, and 4×10^{-3} between $w_2(t)$ and $w_3(t)$. A modified time course $w_1'(t)$ was obtained from $w_1'(t) = (1 - \xi)w_1(t) + \xi w_2(t)$, where parameter ξ controls the degree of the correlation between $w_1'(t)$ and $w_2(t)$. The time course $w_1'(t)$ when $\xi = 0.5$ is shown by the broken line in Fig. 2(a). The correlation coefficient between $w_1'(t)$ and $w_2(t)$ is 0.8 in this case. The simulated magnetic recordings were calculated by assigning $w_1'(t)$, $w_2(t)$, and $w_3(t)$ to the first, second, and third sources, respectively.

The magnetic-field recordings were calculated at 1-ms intervals from zero to 400 ms by using the spherically homogeneous conductor [17] with its center set at $(1, 0, -11)$. White Gaussian noise was then added to the simulated field recordings. The simulated recordings with an SNR of four and with ξ set at zero are shown in Fig. 2(b). Here, the SNR is defined as the ratio of the Frobenius norm of the signal-magnetic-field data matrix to that of the noise matrix, i.e., the ratio of $\sqrt{\langle \|\overline{\boldsymbol{L}}_c \boldsymbol{s}(t)\|^2 \rangle / \langle \|\boldsymbol{n}(t)\|^2 \rangle}$. As we explained in Section V, the SNR of four represents a very poor SNR situation.

B. Signal-Cancellation Experiments

We generated six data sets with the correlation coefficients between the first and second sources, μ, of 0.08, 0.5, 0.6, 0.7, 0.8, and 0.95. The SNR was set at 16. The weight vectors for detecting the x, y, and z components were obtained from (8), and the 3-D reconstruction was performed by using (11). The reconstruction region included the three sources and an area defined by $-2 \leq y \leq 2$ and $-8 \leq z \leq -5$ on plane $x = 1$; this area is displayed in Fig. 3. The interval between the reconstruction grids was 0.1 cm. The results of magnitude-squared average reconstruction for the six values of μ are shown in the six contour maps in Fig. 3, where each contour line represents a relative value of the source magnitude $\sqrt{\langle \tilde{s}(\boldsymbol{r}, t)^2 \rangle}$. The reconstruction results contain three localized sources at the locations

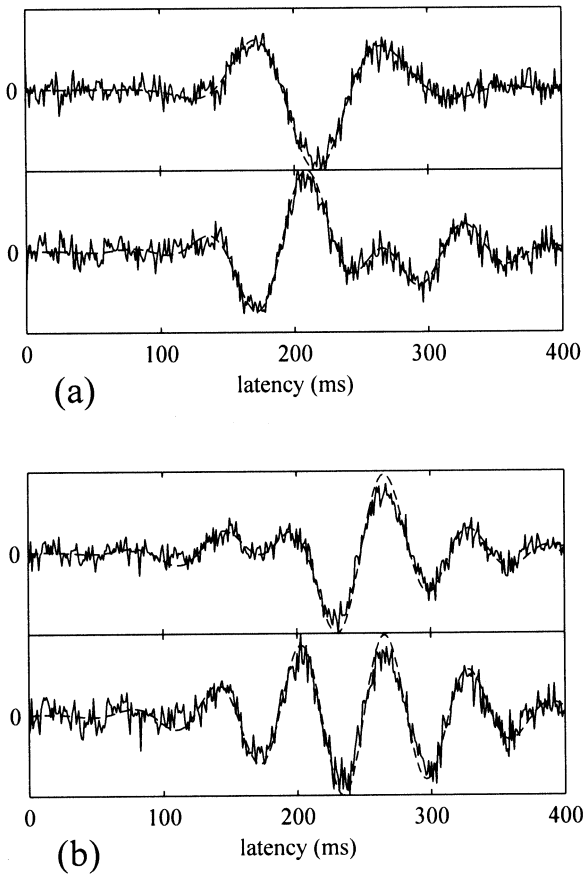

Fig. 7. (a) Predicted time courses and the minimum-variance beamformer outputs of the first and the second sources. The solid lines indicate the beamformer outputs obtained when $\mu = 0.8$ and SNR is equal to four. The broken lines indicate the time courses predicted from (22) or (23). (b) Results of the experiment on time-course retrieval when $\mu = 0.8$ and SNR is equal to four. Solid lines indicate retrieved time courses and broken lines indicate original time courses assumed.

given in Table I. These results, however, are somewhat blurry as a result of noise effects [30].

These contour maps clearly show that, compared with the intensity of the third source, the intensities of the first and the second sources are reduced according to their degree of correlation. This intensity reduction is theoretically predicted in (25) and (26), which indicate that the intensities of the reconstructed sources are reduced by a factor of $\sqrt{(1-\mu^2)}$. Monte Carlo-type experiments were performed to check whether this relationship holds in nonidealistic situations such as when SNR is considerably low. One hundred sets of simulated magnetic recordings were generated with different noise realizations for ten different values of μ. The mean intensity of the reconstructed first source is plotted in Fig. 4. The SNR was set at four. The theoretical trend $\sqrt{(1-\mu^2)}$ is plotted with the broken line, and the error bars show the range of ± 2 standard deviations. In Fig. 4, although a small discrepancy is observed when μ approaches one, the broken line is generally overlapped with the plots from the Monte Carlo experiments, indicating that the theoretical relationship holds well even at the low SNR situation.

According to the trend $\sqrt{(1-\mu^2)}$, the intensity reduction is less than twenty percent, unless the correlation coefficient exceeds 0.6, and 60% of the original source intensity is still maintained when the correlation reaches 0.8. Therefore, as far as the signal intensity reduction is concerned, no serious influences arise from sources with weak or medium degrees of correlation ($\mu \leq 0.6$). Even when sources are significantly correlated ($\mu \sim 0.7$–0.8), the beamformer can still reconstruct such sources if their intensities are strong enough to overcome the signal cancellation. The results in Fig. 3 demonstrated this fact, i.e., there is no large difference between the reconstructed sources when $\mu = 0$ and $\mu = 0.6$.

C. Estimation of Cross-Correlation Coefficient

The correlation coefficient between the first and second sources was estimated from (27) using beamformer outputs $\tilde{s}(\boldsymbol{r}_1, t)$ and $\tilde{s}(\boldsymbol{r}_2, t)$; these outputs are obtained using (8) and (11). To investigate the influence of noise on the accuracy of the calculated correlation coefficient, we performed Monte Carlo-type experiments in which 100 values of the correlation coefficient between the first and second sources were calculated using the 100 sets of simulated magnetic recordings generated with different noise realizations. Such experiments were repeated for five values of SNR, and the results are plotted in Fig. 5 for μ of 0.5 and 0.8. In this figure, the error bars show the range between ± 2 standard deviations. This plot shows that the influence of the noise on the estimated correlation coefficient is generally very small. The estimated correlation coefficient is biased and the average of the estimates is slightly smaller than the true value when SNR equals three. However, this bias is very small and is less than 5% for the whole SNR range used for the experiments.

D. Errors in Time-Course Estimate and Original Time Course Retrieval

Reconstructed time courses of the three source activities are shown in Fig. 6. The SNR was set at four in this experiment. The results in Fig. 6(a)–(d), respectively, correspond to $\mu = 0.08$, $\mu = 0.4$, $\mu = 0.6$, and $\mu = 0.8$. The solid lines indicate the beamformer outputs obtained from (8) and (11), and the broken lines indicate the original time courses assumed in the numerical experiments. When μ is small, original time courses can be retrieved as beamformer outputs. However, as μ increases, the reconstructed time courses become distorted because of the interference from the other correlated source. This distortion is evident when $\mu = 0.6$ and $\mu = 0.8$; it is small but still discernible when $\mu = 0.4$.

These distorted beamformer outputs can be theoretically predicted from (22) and (23). The predicted beamformer outputs and the actual outputs for $\mu = 0.8$ are shown in Fig. 7(a). The outputs predicted from (22) and (23) are shown by broken lines, and the beamformer outputs are shown by solid lines. The solid and broken lines are nearly perfectly overlapped, indicating that (22) and (23) are valid even for an SNR as low as four. We next performed a time-course retrieval experiment. In this experiment, the true time courses were retrieved by using the beamformer outputs $\tilde{s}(\boldsymbol{r}_1, t)$ and $\tilde{s}(\boldsymbol{r}_2, t)$ with (32). The results of

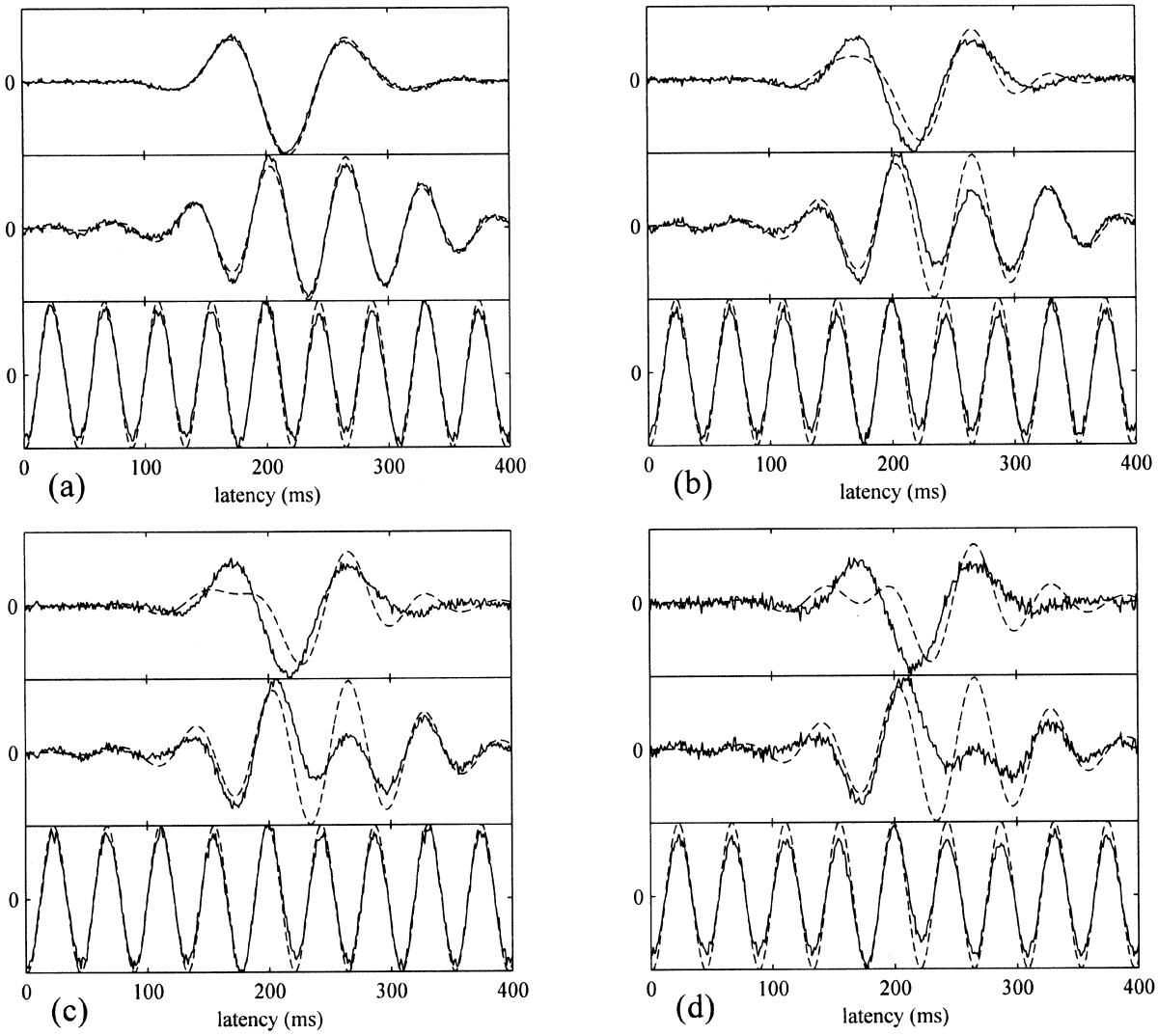

Fig. 8. Results from the eigenspace-projection beamformer given by (9), (11), and (13). The same simulated recordings as used for obtaining the results in Fig. 6 were again used. Time course outputs for the three sources when SNR is equal to four and (a) $\mu = 0.08$, (b) $\mu = 0.4$, (c) $\mu = 0.6$, and (d) $\mu = 0.8$. Time courses from the first to third sources are shown from top to bottom. The solid lines indicate the beamformer outputs and the broken lines indicate the original time courses assumed.

this experiment are shown in Fig. 7(b). In this figure, the retrieved and true time courses are nearly perfectly overlapped, although a small discrepancy exists between the two time courses due probably to noise effects.

We also applied the eigenspace-projection beamformer to the same data sets used for obtaining the results in Fig. 6. The weight vector was obtained from (8) and (13), and the reconstruction was performed by using (11). Reconstructed time courses of the three source activities are shown in Fig. 8, in which the results in (a)–(d) correspond respectively to $\mu = 0.08$, $\mu = 0.4$, $\mu = 0.6$, and $\mu = 0.8$. These time courses are, in principle, identical to those in Fig. 6, although the noise was considerably reduced by the eigenspace projection [26]. The predicted beamformer outputs and the actual outputs for $\mu = 0.8$ are shown in Fig. 9(a), and the retrieved and true time courses are shown in Fig. 9(b). In Fig. 9(a), the predicted outputs are nearly perfectly overlapped with the actual outputs. In Fig. 9(b), the retrieved and true time courses are overlapped. These results confirm that the prediction using (22) and (23) and the time-course retrieval using (32) are also effective for the eigenspace-projection beamformer.

V. Discussions

We have shown that when two sources are correlated, the cross-correlation coefficient can be accurately estimated from the beamformer outputs. However, if a third correlated source exists, the accuracy of the estimated correlation coefficient is affected by this source. This influence can be evaluated from (31). When $\mu_{13} \sim \mu_{23}$, this equation can be simplified as

$$\tilde{\mu}_{12} = \frac{|\mu_{12} - \mu_I^2|}{(1 - \mu_I^2)} \tag{35}$$

where μ_I ($=\mu_{13} = \mu_{23}$) is the correlation of the target sources (the first and second sources) with the interference source (the third source). This equation is plotted for the three values of the target correlation μ_{12} in Fig. 10. This figure shows that even when an additional correlated source exists, the errors due to

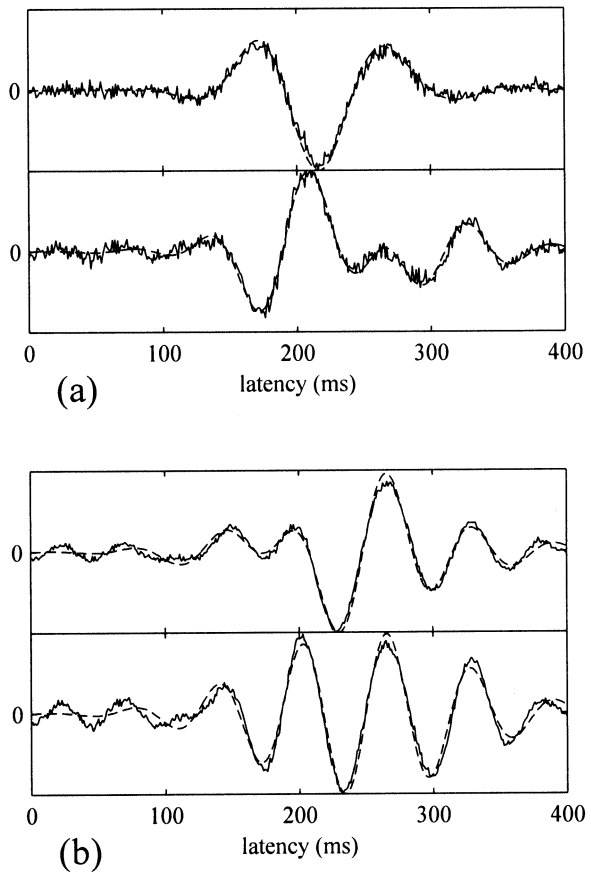

Fig. 9. (a) Predicted time courses and eigenspace-projection beamformer outputs of the first and the second sources. Solid lines indicate the beamformer outputs obtained when $\mu = 0.8$ and SNR is equal to four. Broken lines indicate the time courses predicted from (22) and (23). (b) Results of the experiment on time course retrieval when $\mu = 0.8$ and SNR is equal to four. Solid lines indicate retrieved time courses and broken lines indicate original time courses.

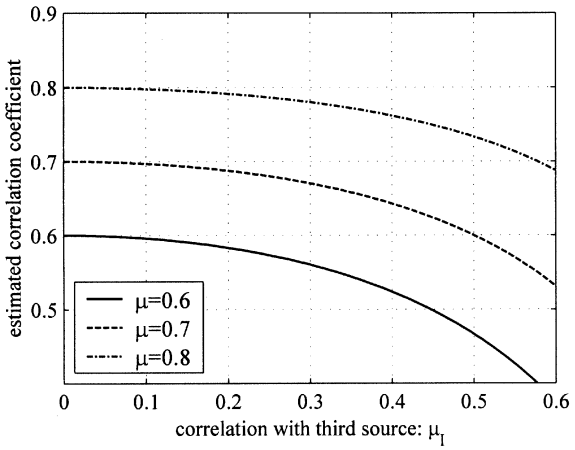

Fig. 10. Effects of a third correlated source on the estimates of the target correlation coefficient. Dotted, broken, and solid lines correspond to the estimate when $\mu = 0.8$, $\mu = 0.7$, and $\mu = 0.6$, respectively.

this interference source are less than 10%, unless μ_I exceeds eighty percent of μ_{12}. Therefore, it is generally true that if the correlation with the interference source is not as strong as the correlation between the target sources, a reasonably accurate target-source correlation coefficient can be obtained.

One may notice that, in Figs. 6 and 8, the output for the first source has a time course that is very similar to $w_1(t)$. This similarity can be explained as follows. The case of $\mu = 0.8$ is considered here. In this case, the time course of the first source $w_1'(t)$ was derived from $w_1'(t) = 0.5w_1(t) + 0.5w_2(t)$. Since the coefficient of $(\alpha_1/\alpha_2)\mu$ in (22) is equal to 0.53, the output $\tilde{\boldsymbol{s}}(\boldsymbol{r}_1, t)$ is expressed as $\tilde{\boldsymbol{s}}(\boldsymbol{r}_1, t) \propto w_1'(t) - 0.53w_2(t) = w_1(t) - 0.03w_2(t)$. This indicates that the beamformer reconstruction coincidentally removed nearly all the $w_2(t)$ components and $\tilde{s}(\boldsymbol{r}_1, t)$ becomes very close to $w_1(t)$. On the other hand, since the coefficient of $(\alpha_2/\alpha_1)\mu$ is equal to 1.2, the output of the second-source time course is equal to $\tilde{s}(\boldsymbol{r}_2, t) \propto w_2(t) - 1.2w_1'(t) = 0.6w_1(t) + 0.4w_2(t)$. Therefore, output $\tilde{s}(\boldsymbol{r}_2, t)$ is considerably distorted by the existence of the $w_1(t)$ component.

In our numerical experiments in Section IV, we used an SNR of four to show that the results of our analysis in Section III, which is based on a high-SNR assumption, are still valid for low-SNR cases. In the following, we show that an SNR of four is a reasonable assumption for simulating low-SNR situations. As pointed out in Section II-A, noise with external origins such as background brain activities is considered as a part of the signals in our analysis. Thus, the noise referred to here indicates only that with internal origins such as noise from the probe coils, SQUIDs, and the associated electronics. The level of such noises in typical modern neuromagnetic instruments is known to be generally less than 5 fT/$\sqrt{\text{Hz}}$ [1], [31]. On the other hand, the peak amplitude of a typical neuromagnetic signal is known to be 50–500 fT [1]. A simple case, where the signal has a sinusoidal waveform with a peak amplitude of 200 fT, is considered here. The bandwith of the data acquisition is assumed to be 200 Hz, so the SNR defined from the Frobenius norm is calculated as $200/50/\sqrt{2 \times 2} = 2$. This SNR can be improved by signal averaging for evoked neuromagnetic measurements with a factor equal to the square-root of the number of averagings. It can, therefore, be concluded that an SNR of four is almost equal to the SNR of the evoked neuromagnetic measurements with a very few number of averagings, and this SNR value represents very low-SNR situations.

One influence of correlated sources that is not discussed in this paper is the degradation of the spatial resolution. The spatial resolution is degraded by the source correlation, but the degradation is generally small when the sources have a weak or medium degree of correlation, as demonstrated in Fig. 3. That is, an image blur can be observed, but it is not significant in Fig. 3(a)–(e) ($\mu \leq 0.8$). We are currently investigating the factors that determine the spatial resolution in the adaptive beamformer neuromagnetic reconstruction. The results of these investigations, including the influence of the source correlation, will be published in the near future.

In summary, we analyzed the effects of correlated sources on the reconstruction results of MEG adaptive beamformer techniques. Two major influences were found: signal-intensity reductions and distortions in the time-course estimate. Our numerical experiments showed that the theoretical relationship between signal intensity and source correlation holds in nonidealistic situations such as when SNR is considerably low. Indeed, as far as the signal intensity is concerned, no serious influences

arise from sources with weak or medium degrees of correlation ($\mu \leq 0.5$). However, distortion in time-course estimates is discernible even for such correlated sources. We also developed a method of correcting the time-course distortion for two-source correlation, and our numerical experiments demonstrate that the distortion can be almost perfectly corrected.

APPENDIX I

This appendix shows the derivation of (16), which was originally derived by Zoltowski [27]. We define the matrix $\boldsymbol{C}$ as $\boldsymbol{C} = \overline{\boldsymbol{L}}_c \boldsymbol{R}_s \overline{\boldsymbol{L}}_c^T$. Then, using (5), we get the relationship $\boldsymbol{R}_b = \boldsymbol{C} + \sigma^2 \boldsymbol{I}$. Therefore, when the SNR is so high that noise can be neglected, the relationship $\boldsymbol{R}_b \approx \boldsymbol{C}$ holds, and we get

$$\begin{aligned} \boldsymbol{R}_b^{-1} \approx \boldsymbol{C}^+ &= \left(\overline{\boldsymbol{L}}_c \boldsymbol{R}_s \overline{\boldsymbol{L}}_c^T\right)^+ = \left(\overline{\boldsymbol{L}}_c^T\right)^+ \boldsymbol{R}_s^+ \overline{\boldsymbol{L}}_c^+ \\ &= \left(\overline{\boldsymbol{L}}_c^+\right)^T \boldsymbol{R}_s^{-1} \overline{\boldsymbol{L}}_c^+. \end{aligned} \tag{36}$$

Here, $\overline{\boldsymbol{L}}_c^+$ indicates the pseudoinverse of $\overline{\boldsymbol{L}}_c$ defined as $\overline{\boldsymbol{L}}_c^+ = [\overline{\boldsymbol{L}}_c^T \overline{\boldsymbol{L}}_c] \overline{\boldsymbol{L}}_c^T$. Regarding (36), we also assume that $\boldsymbol{R}_s$ is nonsingular, and we use the fact that the transpose and the pseudoinverse operations are interchangeable. We apply the formula $\overline{\boldsymbol{L}}_c^+ \boldsymbol{l}(\boldsymbol{r}_j) = \mathbf{u}_j$, where $\boldsymbol{u}_j$ is the $M \times 1$ vector that has all elements equal to zero except for the jth element that is equal to one. Using this formula and (36), we obtain

$$\begin{aligned} \boldsymbol{w}^T(\boldsymbol{r}_p)\boldsymbol{l}(\boldsymbol{r}_q) &\fallingdotseq \frac{\boldsymbol{l}^T(\boldsymbol{r}_p)\left[\overline{\boldsymbol{L}}_c^+\right]^T \boldsymbol{R}_s^{-1} \overline{\boldsymbol{L}}_c^+ \boldsymbol{l}(\boldsymbol{r}_q)}{\boldsymbol{l}^T(\boldsymbol{r}_p)\left[\overline{\boldsymbol{L}}_c^+\right]^T \boldsymbol{R}_s^{-1} \overline{\boldsymbol{L}}_c^+ \boldsymbol{l}(\boldsymbol{r}_p)} \\ &= \frac{\boldsymbol{u}_p^T \boldsymbol{R}_s^{-1} \boldsymbol{u}_q}{\boldsymbol{u}_p^T \boldsymbol{R}_s^{-1} \boldsymbol{u}_p} = \frac{[\boldsymbol{R}_s^{-1}]_{pq}}{[\boldsymbol{R}_s^{-1}]_{pp}}. \end{aligned} \tag{37}$$

Note that this equation exactly holds when noise can be neglected. Since $\boldsymbol{E}_S \boldsymbol{E}_S^T \boldsymbol{R}_b = \boldsymbol{C}$, (37) is also valid for the eigenspace-projection beamformer mentioned in Section II-D.

One vital assumption in the argument above is that of the low-rank signal; i.e., the assumption that the number of signal sources Q is less than the number of sensors M. If this assumption does not hold, $\overline{\boldsymbol{L}}_c^+ \boldsymbol{l}(\boldsymbol{r}_j)$ is not equal to $\boldsymbol{u}_j$ and (37) cannot be derived. However, since the number of sensors in commercially available neuromagnetometers has increased constantly over the last ten years and the latest neuromagnetometers are equipped with 200–300 sensor channels, the low-rank-signal assumption should hold for most neuromagnetic measurements.

APPENDIX II

This appendix shows that the magnitude of the cross coherence in the frequency domain can also be estimated using the outputs from the frequency-domain beamformer implementation. We define the Fourier transform of the measurement vector $\boldsymbol{b}(t)$ as a vector $\boldsymbol{\beta}(f) = [\beta_1(f), \ldots, \beta_M(f)]^T$, where $\beta_m(f)$ is the Fourier spectrum of the mth-channel recording $b_m(t)$. We also define the Fourier transform of the source-activity vector as $\boldsymbol{\theta}(f) = [\theta(\boldsymbol{r}_1, f), \ldots, \theta(\boldsymbol{r}_Q, f)]^T$ where $\theta(\boldsymbol{r}_q, f)$ is the Fourier spectrum of the qth source magnitude $s_q(t)$. Let us define the cross-spectrum matrix of the measured data as $\boldsymbol{\Gamma}_\beta$: $\boldsymbol{\Gamma}_\beta(f) = \langle \boldsymbol{\beta}(f) \boldsymbol{\beta}^H(f) \rangle$, where the superscript H indicates the Hermitian transpose. The estimated Fourier spectrum of the source activity at $\boldsymbol{r}$, $\tilde{\theta}(\boldsymbol{r}, f)$, is obtained as

$$\tilde{\theta}(\boldsymbol{r}, f) = \boldsymbol{w}^T(\boldsymbol{r}) \boldsymbol{\beta}(f) \tag{38}$$

where the weight vector $\boldsymbol{w}^T(\boldsymbol{r})$ is given by

$$\boldsymbol{w}(\boldsymbol{r}) = \frac{\boldsymbol{\Gamma}_\beta^{-1}(f) \boldsymbol{l}(\boldsymbol{r})}{\boldsymbol{l}^T(\boldsymbol{r}) \boldsymbol{\Gamma}_\beta^{-1}(f) \boldsymbol{l}(\boldsymbol{r})}. \tag{39}$$

When the first and second sources have a coherence value γ at the frequency f, we get the relationship

$$\tilde{\theta}(\boldsymbol{r}_1, f) = \theta(\boldsymbol{r}_1, f) - \left(\frac{\nu_1}{\nu_2}\gamma\right) \theta(\boldsymbol{r}_2, f) \tag{40}$$

$$\tilde{\theta}(\boldsymbol{r}_2, f) = \theta(\boldsymbol{r}_2, f) - \left(\frac{\nu_2}{\nu_1}\gamma\right) \theta(\boldsymbol{r}_1, f) \tag{41}$$

where ν_j^2 is the power spectrum of the jth source at f. Then, substituting (40) and (41) into

$$\tilde{\gamma} = \frac{\left|\left\langle \tilde{\theta}(\boldsymbol{r}_1, f) \tilde{\theta}^H(\boldsymbol{r}_2, f) \right\rangle\right|}{\sqrt{\left\langle \tilde{\theta}(\boldsymbol{r}_1, f)^2 \right\rangle \left\langle \tilde{\theta}(\boldsymbol{r}_2, f)^2 \right\rangle}} \tag{42}$$

leads to

$$\tilde{\gamma} = \frac{|\nu_1 \nu_2 (\gamma^3 - \gamma)|}{\sqrt{\nu_1^2 (1 - \gamma^2) \nu_2^2 (1 - \gamma^2)}} = |\gamma| \tag{43}$$

where $\tilde{\gamma}$ is the estimated magnitude coherence. Equation (43) indicates that the accurate estimate of the magnitude coherence can be obtained by substituting the outputs of the beamformer into (42). It should be noted that the analysis in this appendix provides a theoretical validation of the method recently proposed by Gross *et al.* [15].

APPENDIX III

This appendix presents the inverse of the source covariance matrix in the case of a three-source correlation. We assume that the first, second, and third sources are mutually correlated. The correlation coefficients of these sources are denoted as μ_{12}, μ_{13},

$$\overline{\boldsymbol{R}}_s^{-1} = \frac{1}{|\overline{\boldsymbol{R}}_s|} \begin{bmatrix} \alpha_2^2 \alpha_3^2 (1 - \mu_{23}^2) & \alpha_1 \alpha_2 \alpha_3^2 (\mu_{13}\mu_{23} - \mu_{12}) & \alpha_1 \alpha_2^2 \alpha_3 (\mu_{12}\mu_{23} - \mu_{13}) \\ \alpha_1 \alpha_2 \alpha_3^2 (\mu_{13}\mu_{23} - \mu_{12}) & \alpha_1^2 \alpha_3^2 (1 - \mu_{13}^2) & \alpha_1^2 \alpha_2 \alpha_3 (\mu_{12}\mu_{13} - \mu_{23}) \\ \alpha_1 \alpha_2^2 \alpha_3 (\mu_{12}\mu_{23} - \mu_{13}) & \alpha_1^2 \alpha_2 \alpha_3 (\mu_{12}\mu_{13} - \mu_{23}) & \alpha_1^2 \alpha_2^2 (1 - \mu_{12}^2) \end{bmatrix} \tag{45}$$

and μ_{23}. In the source-activity covariance matrix $\boldsymbol{R}_s$, the submatrix related to the three correlated sources is denoted as $\overline{\boldsymbol{R}}_s$. This matrix is expressed as

$$\overline{\boldsymbol{R}}_s = \begin{bmatrix} \alpha_1^2 & \mu_{12}\alpha_1\alpha_2 & \mu_{13}\alpha_1\alpha_2 \\ \mu_{12}\alpha_1\alpha_2 & \alpha_2^2 & \mu_{23}\alpha_2\alpha_3 \\ \mu_{13}\alpha_1\alpha_3 & \mu_{23}\alpha_2\alpha_3 & \alpha_3^2 \end{bmatrix}. \quad (44)$$

Its inverse is expressed as shown in (45) at the bottom of the previous page, where $|\overline{\boldsymbol{R}}_s|$ indicates the determinant of $\overline{\boldsymbol{R}}_s$ and is given by

$$|\overline{\boldsymbol{R}}_s| = \alpha_1^2\alpha_2^2\alpha_3^2(1 - \mu_{12}^2 - \mu_{13}^2 - \mu_{23}^2 + 2\mu_{12}\mu_{13}\mu_{23}). \quad (46)$$

REFERENCES

[1] M. Hämäläinen, R. Hari, R. J. IImoniemi, J. Knuutila, and O. V. Lounasmaa, "Magnetoencephalography—Theory, instrumentation, and applications to noninvasive studies of the working human brain," *Rev. Mod. Phys.*, vol. 65, pp. 413–497, 1993.

[2] T. P. L. Roberts, D. Poeppel, and H. A. Rowley, "Magnetoencephalography and magnetic source imaging," *Neuropsych., Neuropsych., Behav. Neurology*, vol. 11, pp. 49–64, 1998.

[3] B. D. van Veen and K. M. Buckley, "Beamforming: A versatile approach to spatial filtering," *IEEE Acoust. Speech Signal Processing Mag.*, vol. 5, pp. 4–24, Apr. 1988.

[4] S. E. Robinson and D. F. Rose, "Current source image estimation by spatially filtered MEG," in *Biomagnetism Clinical Aspects*, M. Hoke *et al.*, Eds. New York: Elsevier, 1992, pp. 761–765.

[5] S. E. Robinson and J. Vrba, "Functional neuroimaging by synthetic aperture magnetometry (SAM)," in *Recent Advances in Biomagnetism*, T. Yoshimoto *et al.*, Eds. Sendai, Japan: Tohoku Univ. Press, 1999, pp. 302–305.

[6] J. Gross and A. A. Ioannides, "Linear transformations of data space in MEG," *Phys. Med. Biol.*, vol. 44, pp. 2081–2097, 1999.

[7] K. Sekihara, S. S. Nagarajan, D. Poeppel, A. Marantz, and Y. Miyashita, "Reconstructing spatio–temporal activities of neural sources using an MEG vector beamformer technique," *IEEE Trans. Biomed. Eng.*, vol. 48, pp. 760–771, July 2001.

[8] I. Hashimoto, T. Kimura, Y. Iguchi, R. Takino, and K. Sekihara, "Dynamic activation of distinct cytoarchitectonic areas of the human SI cortex after median nerve stimulation," *NeuroReport*, vol. 12, pp. 1891–1897, 2001.

[9] I. Hashimoto, K. Sakuma, T. Kimura, Y. Iguchi, and K. Sekihara, "Serial activation of distinct cytoarchitectonic areas of the human SI cortex after posterior tibial nerve stimulation," *NeuroReport*, vol. 12, pp. 1857–1862, 2001.

[10] M. S. Hämäläinen and R. J. Ilmoniemi, "Interpreting measured magnetic fields of the brain: Estimates of current distributions," Helsinki Univ. Technol., Helsinki, Finland, Tech. Rep. TKK-F-A559, 1984.

[11] K. Sekihara and S. S. Nagarajan, "Neuromagnetic source reconstruction and inverse modeling," in *Modeling and Imaging of Bioelectric Activity—Principles and Applications*, B. He, Ed. Norwell, MA: Kluwer, to be published.

[12] K. Sekihara and B. Scholz, "Generalized Wiener estimation of three-dimensional current distribution from biomagnetic measurements," in *Biomag 96: Proc. 10th Int. Conf. Biomagnetism*, C. J. Aine *et al.*, Eds., 1996, pp. 338–341.

[13] A. S. Gevins, S. L. Bressler, N. H. Morgan, B. A. Cutillo, R. M. White, D. S. Greer, and J. Illes, "Event-related covariances during a bimanual visuomotor task. I. Methods and analysis of stimulus- and response-locked data," *Electroenceph. Clin. Neurophysiol.*, vol. 74, pp. 58–75, 1989.

[14] J. Sarnthein, H. Petsche, P. Rappelsberger, G. L. Shaw, and A. von Stein, "Synchronization between prefrontal and posterior association cortex during human working memory," *Proc. Nat. Acad. Sci.*, vol. 95, pp. 7092–7096, 1998.

[15] J. Gross, J. Kujara, M. Hämäläinen, L. Timmermann, A. Schnitzler, and R. Salmelin, "Dynamic imaging of coherent sources: Studying neural interactions in the human brain," *Proc. Nat. Acad. Sci.*, vol. 98, pp. 694–699, 2001.

[16] W. Singer, "Neuronal synchrony: A versatile code for the definition of relations," *Neuron*, vol. 24, pp. 49–65, 1999.

[17] J. Sarvas, "Basic mathematical and electromagnetic concepts of the biomagnetic inverse problem," *Phys. Med. Biol.*, vol. 32, pp. 11–22, 1987.

[18] A. Paulraj, B. Ottersten, R. Roy, A. Swindlehurst, G. Xu, and T. Kailath, "Subspace methods for directions-of-arrival estimation," in *Handbook of Statistics*, N. K. Bose and C. R. Rao, Eds. Amsterdam, The Netherlands: Elsevier, 1993, pp. 693–739.

[19] R. O. Schmidt, "A signal subspace approach to multiple emitter location and spectral estimation," Ph.D. dissertation, Dept. Elect. Eng., Stanford Univ., Stanford, CA, 1981.

[20] L. L. Scharf, *Statistical Signal Processing: Detection, Estimation, and Time Series analysis*. Reading, MA: Addison-Wesley, 1991.

[21] D. H. Johnson and D. E. Dudgeon, *Array Signal Processing: Concepts and Techniques*. Englewood Cliffs, NJ: Prentice-Hall, 1993.

[22] J. Capon, "High-resolution frequency wavenumber spectrum analysis," *Proc. IEEE*, vol. 57, pp. 1408–1419, Aug. 1969.

[23] J. C. Mosher, P. S. Lewis, and R. M. Leahy, "Multiple dipole modeling and localization from spatio–temporal MEG data," *IEEE Trans. Biomed. Eng.*, vol. 39, pp. 541–557, June 1992.

[24] M. E. Spencer, R. M. Leahy, J. C. Mosher, and P. S. Lewis, "Adaptive filters for monitoring localized brain activity from surface potential time series," in *Conf. Rec. 26th Ann. Asilomer Conf. Signals, Systems, Computers*, Nov. 1992, pp. 156–161.

[25] B. D. van Veen, W. van Drongelen, M. Yuchtman, and A. Suzuki, "Localization of brain electrical activity via linearly constrained minimum variance spatial filtering," *IEEE Trans. Biomed. Eng.*, vol. 44, pp. 867–880, Sept. 1997.

[26] K. Sekihara, S. S. Nagarajan, D. Poeppel, A. Marantz, and Y. Miyashita, "Application of an MEG eigenspace beamformer to reconstructing spatio–temporal activities of neural sources," *Human Brain Mapping*, vol. 15, pp. 199–215, 2002.

[27] M. D. Zoltowski, "On the performance analysis of the MVDR beamformer in the presence of correlated interference," *IEEE Trans. Signal Processing*, vol. 36, pp. 945–947, June 1988.

[28] B. Widrow, K. M. Duval, R. P. Gooch, and W. C. Newman, "Signal cancellation phenomena in adaptive antennas: Causes and cures," *IEEE Trans. Antennas Propagat.*, vol. AP-30, pp. 469–478, May 1982.

[29] A. Paulraj, V. U. Reddy, and T. Kailath, "Analysis of signal cancellation due to multipath in optimum beamformers for moving arrays," *IEEE J. Ocean. Eng.*, vol. OE-12, pp. 163–172, Jan. 1987.

[30] H. Cox, "Resolving power and sensitivity to mismatch of optimum array processors," *J. Acoust. Soc. Amer.*, vol. 54, pp. 771–785, 1973.

[31] J. Vrba, "SQUID gradiometers in real environments," in *SQUID Sensors: Fundamentals, Fabrication and Applications*, H. Weinstock, Ed. Norwell, MA: Kluwer, 1996, pp. 117–178.

Kensuke Sekihara received the M.S. and Ph.D. degrees from the Tokyo Institute of Technology, Tokyo, Japan, in 1976 and 1987, respectively.

From 1976 to 2000, he was with Central Research Laboratory, Hitachi, Ltd., Tokyo, Japan. He was a visiting Research Scientist at Stanford University, Stanford, CA, from 1985 to 1986, and at Basic Development, Siemens Medical Engineering, Erlangen, Germany, from 1991 to 1992. From 1996 to 2000, he was with the "Mind Articulation" Research Project sponsored by the Japan Science and Technology Corporation. He is currently a Professor at Tokyo Metropolitan Institute of Technology, Tokyo, Japan. His research interests include biomagnetic inverse problems, and statistical estimation theory, especially its application to functional neuroimaging.

Dr. Sekihara is a Member of the IEEE Medicine and Biology Society and the IEEE Signal Processing Society.

Srikantan S. Nagarajan received the B.S. degree in electrical engineering from the University of Madras, Madras, India, and the M.S. and Ph.D. degrees from the Department of Biomedical Engineering, Case Western Reserve University, Cleveland, OH, in 1993 and 1995, respectively.

From 1995 to 1998, he was a Postdoctoral Fellow at the Keck Center for Integrative Neuroscience, the University of California, San Francisco (UCSF). In 1999, he was a full-time Research Scientist at Scientific Learning Corporation, Berkeley, CA, and an Adjunct Assistant Professor in the Department of Otolaryngology at UCSF. Subsequently, he was an Assistant Professor in the Department of Bioengineering at the University of Utah, Salt Lake City. Currently, he is the Director of the Biomagnetic Imaging Laboratory and an Assistant Professor in the Department of Radiology at UCSF. His research interests in neural engineering include bioelectromagnetism, systems and computational neuroscience, rehabilitation, and statistical signal processing.

David Poeppel received the B.S. and Ph.D. degrees in cognitive neuroscience from the Massachusetts Institute of Technology, Cambridge, in 1990 and 1995, respectively.

Currently, he is an Assistant Professor in the Departments of Linguistics and Biology at the University of Maryland at College Park. His research uses the functional neuroimaging methods magnetoencephalography (MEG), electroencephalography (EEG), positron emission tomography (PET), and functional magnetic resonance imaging (fMRI) to investigate the neural basis of speech and language processing.

Alec Marantz received the B.A. degree in psycholinguistics from Oberlin College, Oberlin, OH, and the Ph.D. degree in linguistics from the Massachusetts Institute of Technology (MIT), Cambridge, in 1978 and 1981, respectively.

He joined the Faculty of MIT in 1990, where he is currently Professor of Linguistics and Head of the Department of Linguistics and Philosophy. His research interests include the syntax and morphology of natural languages, linguistic universals, and the neurobiology of language. He is currently involved in revising morphological theory within linguistics and in exploring MEG techniques to uncover how the brain processes language.